DROACOR®-THERMAL: AUTOMATED TEMPERATURE / EMISSIVITY RETRIEVAL FOR DRONE BASED HYPERSPECTRAL IMAGING DATA

D. Schläpfer[1]*, R. Richter[1], C. Popp[1], P. Nygren[2]

[1]ReSe Applications LLC, CH-9500 Wil, Switzerland - daniel@rese-apps.com, rudolf.richter@rese-apps.com, popp@rese-apps.com
[2] SMAPS Spectral Mapping Services, 20320 Turku, Finland - petri.nygren@smaps.fi

Commission III, WG III/4

KEY WORDS: DROACOR®, UAV Hyperspectral Thermal Imaging, Atmospheric Correction, Mineral Exploration.

ABSTRACT:

Thermal remote sensing from unmanned aerial vehicles is a slowly but steadily growing field of application. New hyperspectral systems operating in the thermal infrared are deployable on such systems and are also usable for ground based monitoring, such as in mining applications. Temperature/emissivity retrieval methods have to be adapted for these new situations. This contribution presents an extension of the Drone Atmospheric Correction method (DROACOR®) for thermal infrared imaging spectroscopy. The method includes an implementation of the semi-automatic normalized emissivity mapping (NEM) method for temperature/emissivity separation. Furthermore, an extension of the method for correction of low emissivity targets, appearing as cold targets in the temperature mapping is introduced. Two examples of DROACOR-thermal processing are presented for a nadir looking drone based and a horizontal ground based data acquisitions are shown. The resulting spectral emissivitiy distributions and temperature mappings are plausible. They are well comparable to spectral library references and allow for the detection of materials only visible in the thermal infrared range.

1. INTRODUCTION

During the last few years, UAV-borne sensors have been widely used in geology, exploration, and agriculture. The hyperspectral sensors usually cover the spectral region visible/ near-infrared (400 - 1000 nm) and short-wave infrared (1000 - 2500 nm). Thermal imaging instruments (7 - 14 μm) are less employed on UAV because they are usually more expensive. Nevertheless, they offer important complementary information to sensors operating in the solar reflective spectrum. There are single-channel broad-band thermal cameras of the FLIR type, e.g., FLIR-Duo (Teledyne FLIR, 2021), and also hyperspectral sensors, e.g., Specim OWL (SPECIM Spectral Imaging Ltd., 2021), ITRES TASI (ITRES Research LImited, 2019), and Telops Hypercam (TELOPS, 2022) covering the 8 - 12 μm region with up to about 100 spectral bands. While airborne data acquisitions usually cover altitudes from 500 m to 5 km above ground, UAV platforms typically operate from 10 m to 500 m above ground at comparatively low costs.

Atmospheric correction for drone imagery has become into focus lately. As more and more high quality systems are mountable on small carriers, physical corrections have become feasible. This led to the development of the drone atmospheric correction software (DROACOR, (Schläpfer et al., 2020)) which is optimized for drone based hyperspectral systems in the 0.4 to 2.5 μm range and may also be used for ground based imaging spectroscopy (Schläpfer et al., 2021). The goal of this contribution is to describe a further addition to DROACOR by extending its functionality into the thermal infrared wavelength range.

For the short optical path of UAV systems, the main atmospheric influence factor in the thermal infrared is water vapor. The aerosol type is negligible due to the long wavelength and it is sufficient to consider a standard aerosol load, e.g. for a visibility of 30 km. We employ the libRadtran radiative transfer code (Mayer et al., 2019) to compute the atmospheric influence functions (transmittance, path radiance, and downward thermal flux). Due to the typically small area coverage of UAV data acquisitions, these functions can be assumed as constant for the image processing. Based on these preconditions, a streamlined temperature-emissivity separation method is shown hereafter.

2. METHOD

In the thermal infrared spectrum the radiative transfer equation can be written as (Kahle et al., 1980):

$$L(\lambda) = L_p(\lambda) + \tau(\lambda)\,\varepsilon(\lambda)\,L_{bb}(\lambda,T) + \tau(\lambda)\;(1-\varepsilon(\lambda))\;F(\lambda)/\pi, \quad (1)$$

where $L,\ L_p,\ F$ are TOA or at-sensor radiance, path radiance, and thermal downwelling flux on the ground, respectively, and ε, τ are the surface emissivity and ground-to-sensor atmospheric transmittance.

Except for the emissivity and L_{bb}, all quantities of equation (1) depend on atmospheric parameters, especially on the water vapor column. For low UAV flight levels the water vapor cannot be retrieved from hyperspectral scenes because the small air volume does not cause a significant reduction in atmospheric transmittance. Therefore, the water vapor column is an external parameter. In most cases, a water vapor measurement is not available, and an estimate has to be given. As an aid, typical values for different altitude profiles of temperature and humidity are provided for standard climatological regions (US, mid-latitude summer, winter, tropical) depending on the site elevation.

According to Planck's equation, the emitted blackbody spectral

* Corresponding author contact: daniel@rese-apps.com

radiance L depends on wavelength λ and temperature T,

$$L_{bb}(\lambda, T) = \frac{2\,h\,c^2}{\lambda^5}\,\frac{1}{exp(h\,c/\lambda\,k_B\,T) - 1}, \qquad (2)$$

where h is Planck's constant, c the speed of light, and k_B the Boltzmann constant. For natural bodies with emissivity $\varepsilon(\lambda)$ the emitted spectral radiance is

$$L(\lambda, \varepsilon, T) = \varepsilon(\lambda)\; L_{bb}(\lambda, T). \qquad (3)$$

The blackbody radiance / temperature can be calculated from Planck's law and the channel spectral response function. Then, $T = f^{-1}(L)$ is calculated as:

$$T = \frac{k_2}{ln\,((k_1/L) + 1)}, \qquad (4)$$

where $k_1,\ k_2$ depend on the channel spectral response function. If we define the effective surface radiance L_s as (i = channel index)

$$L_s(i, T) = \varepsilon(i)\; L_{bb}(i, T) \qquad (5)$$

we obtain

$$L_s(i, T) = \frac{L(i) - L_p(i)}{\tau(i)}\; -\; (1 - \varepsilon(i)) \cdot F(i)/\pi. \qquad (6)$$

The atmospheric correction functions $L_p,\ \tau$, and F are stored in the atmospheric LUT, see section 2.3.

2.1 Normalized Emissivity Method

The normalized emissivity method (NEM, (Realmuto, 1990)) is used for the temperature / emissivity separation This method requires multispectral or hyperspectral thermal bands. First, all channels k are assigned a constant emissivity, e.g. $\varepsilon(k) = 0.99,\ (k = 1, ..., n)$, because the spectral emissivity is usually not known. Equations 5, 6 can then be written as

$$L_{bb}(k, T) = \frac{L(k) - L_p(k)}{\tau(k)\;\varepsilon(k)} + (1 - 1/\varepsilon(k))\; F(k)/\pi, \qquad (7)$$

and the path radiance and transmittance from the atmospheric LUTs are taken for the specified water vapor column, ground elevation, and UAV height above ground to calculate the blackbody surface radiance. Then a loop over all bands k is executed to calculate the blackbody surface temperature (eq. 4) for each pixel $T_{bb}(x, y, k)$ and the pixel (blackbody) temperature is defined as the the maximum temperature of all bands:

$$T_{max}(x, y) = max\{T_{bb}(x, y, k)\} \quad (k = 1, ..., n). \qquad (8)$$

The result is a spectrum of blackbody surface temperature and the maximum temperature of all bands $T_{max}(x, y)$ is selected per pixel.

The last step is the calculation of the emissivity map for each channel $\varepsilon(x, y, k)$ using the temperature T_{max}. Omitting the spatial coordinates and solving equation 1 for $\varepsilon(k)$ we get

$$\varepsilon(k) = \frac{\{L(k) - L_p(k)\}/\tau(k) - F(k)/\pi}{L_{bb}(T_{max}) - F(k)/\pi} \qquad (9)$$

The knowledge of the main atmospheric parameter (water vapor column) determines the accuracy of the temperature and emissivity retrieval.

2.2 "Cold" Pixel Processing

Low emissivity areas in thermal scenes cause low radiance values (eq. 5) and thus low brightness temperatures. And a low temperature for a given radiance yields a high emissivity. The "cold" pixel method detects these pixels and iterates the temperature / emissivity calculation.

In urban applications, only a small percentage of pixels will be considered as "cold", e.g., surfaces with a metal or glass roof. A somewhat larger percentage might be encountered in outcrops of mineral exploration, i.e., rock formations that appear at the surface of the ground, since many rock types have low emissivities.

Therefore, the definition of "cold" implicates a larger deviation from the average scene temperature based on some threshold and the following steps are executed:

1. The surface radiance L_s is calculated assuming $\varepsilon(10.1\mu m) = 1$. A channel around 10.1 μm is selected to minimize the influence of atmospheric water vapor. According to equation (6) we obtain

$$L_s(k, T) = \frac{L(k) - L_p(k)}{\tau(k)} \qquad (10)$$

2. Pixels are defined as "cold" if $L_s(x, y) < thc \cdot MEDIAN(L_s)$, where thc is a user-specified threshold, typically from 0.75 to 0.85, and the $MEDIAN$ is evaluated over the scene.

3. Equation (4) defines the "cold" temperature T_{cold} corresponding to the surface radiance $thc \cdot MEDIAN(L_s)$.

$$T_{cold} = \frac{k_2}{ln\,((k_1/thc \cdot MEDIAN(L_s)) + 1)} \qquad (11)$$

4. The surface brightness temperature of the cold pixels is iterated as

$$T_{cold,new}(x, y) = T_{cold}(x, y) + T_{av} - T_{cold,av} \qquad (12)$$

   This equation raises the average temperature of the cold pixels $T_{cold,av}$ to the scene-average temperature T_{av}, while still retaining the temperature variation of the cold areas.

5. A transition zone 'cold-to-normal' of width 1 pixel is defined where scene temperatures are averaged over 3×3 pixels (cold pixel in the center) to get a smoother transition region.

6. If cold pixels were found, a corresponding mask is created, where the cold pixels are coded with 200, transition pixels with 100, and all others with 0.

7. The emissivity spectrum of the cold pixels is updated in the NEM method employing $T_{max}(x, y) = T_{cold,new}(x, y)$, where T_{max} is the maximum channel temperature per pixel.

The resulting images show a realistic temperature in combination with an improved emissivities. Compare Fig. 5 for a practical example.

2.3 LUT Parameters

The spectral processing parameters are calculated with the LibRadtran radiative transfer code (Mayer et al., 2019) and are stored in an atmospheric look-up-table (LUT). It covers the spectrum 7 - 14 μm and has a high spectral sampling distance of 1 nm and full width at half max FWHM = 2 nm. It also supports a large range of ground elevations and UAV flight altitudes, see Table 1. It contains the functions L_p, τ, F of equation (1) and these are convolved with the spectral channel response functions of the specified sensor. The visibility is set to 30 km for all LUT entries as the influence of aerosols is small in the thermal infrared.

Property	Parameter Range
spectral range	7 - 14 μm
SSD, FWHM	1.0, 2.0 nm
ground elevations	0, 500, 1000, 2000, 4000 m a.s.l.
UAV altitudes	10, 100, 200, 500, 1000, 2000 m, 3000, 4000, 5000 m above ground
visibility	30 km
water vapor columns	0.2 - 5 cm, for sea level
scan angles	0, 30° (0=nadir)

Table 1. Specifications of the generic LUT used for emissivity retrieval.

The Figure 1 presents a comparison of two critical atmospheric radiative transfer functions (path radiance and transmittance) between MODTRAN and LibRadtran calculations. The spectra were simulated for a nadir view, ground at sea level, UAV flight altitude 500 m above sea level, atmospheric water vapor column 3 cm, and a hyperspectral instrument with SSD=20 nm, FWHM=40 nm. The RT functions of MODTRAN and LibRadtran agree well and no significant difference between processing outputs are to be expected for standard data acquisitions.

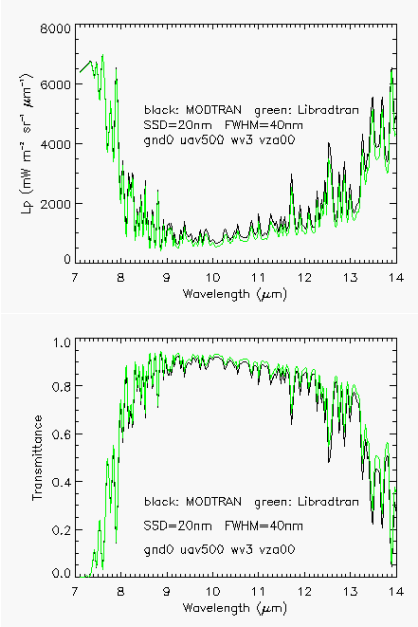

Figure 1. Comparison of MODTRAN and Libradtran simulations of exemplary atmospheric influence functions in the TIR (L_p: path radiance and τ transmittance).

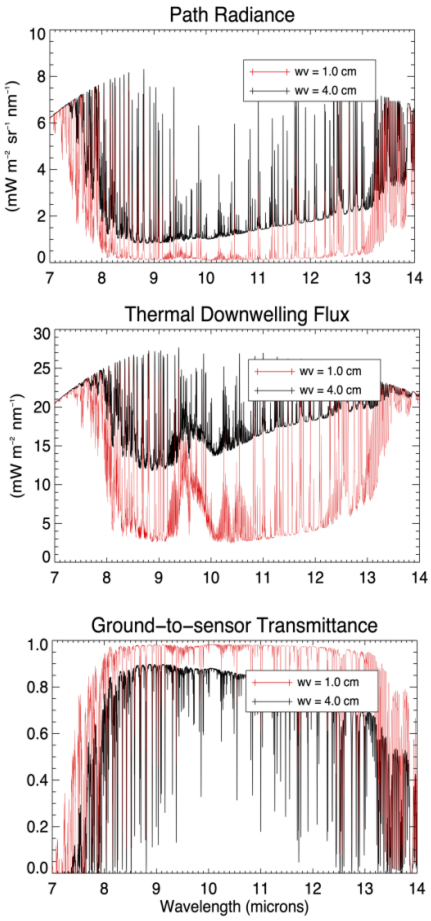

Figure 2. Exemplary atmospheric influence functions in the TIR (from top: path radiance, downward thermal flux, and transmittance). The spectra were simulated for a nadir viewing instrument flying at 500 meters above ground and a surface altitude at sea level. The black lines show libRadtran computations for an atmospheric water vapor column of 1.0 cm und the black lines for water vapor column of 4.0..

The LUT is used to determine the appropriate parameters for Eqs. 7 to 9. Fig. 2 depicts spectra of path radiance, downward thermal flux, and transmittance for a common observation situation of UAV-TIR sensors as stored in the LUT. The flight altitude is set to of 500 meters above ground at sea level and nadir looking. The shown simulations span the range of relatively low and relatively high atmospheric water vapor content (1.0 cm and 4.0 cm). The three atmospheric transfer functions demonstrate the strong impact of water vapor in the thermal infrared between 7 and 14 microns. The path radiance and downwelling flux both increase clearly with increasing water vapor while the transmittance decreases with additional water vapor in the atmosphere. The impact of the ozone absorption band around 9.5 microns is also clearly visible in the thermal downwelling flux plot. Note, that the illustrated curves are shown at the spectral resolution as they are stored in the LUT, namely 1 nm. Usually, those spectra are first convolved with the specific spectral response functions of the instrument before being applied, for example to equation 4 (c.f. Flow chart in Figure 4).

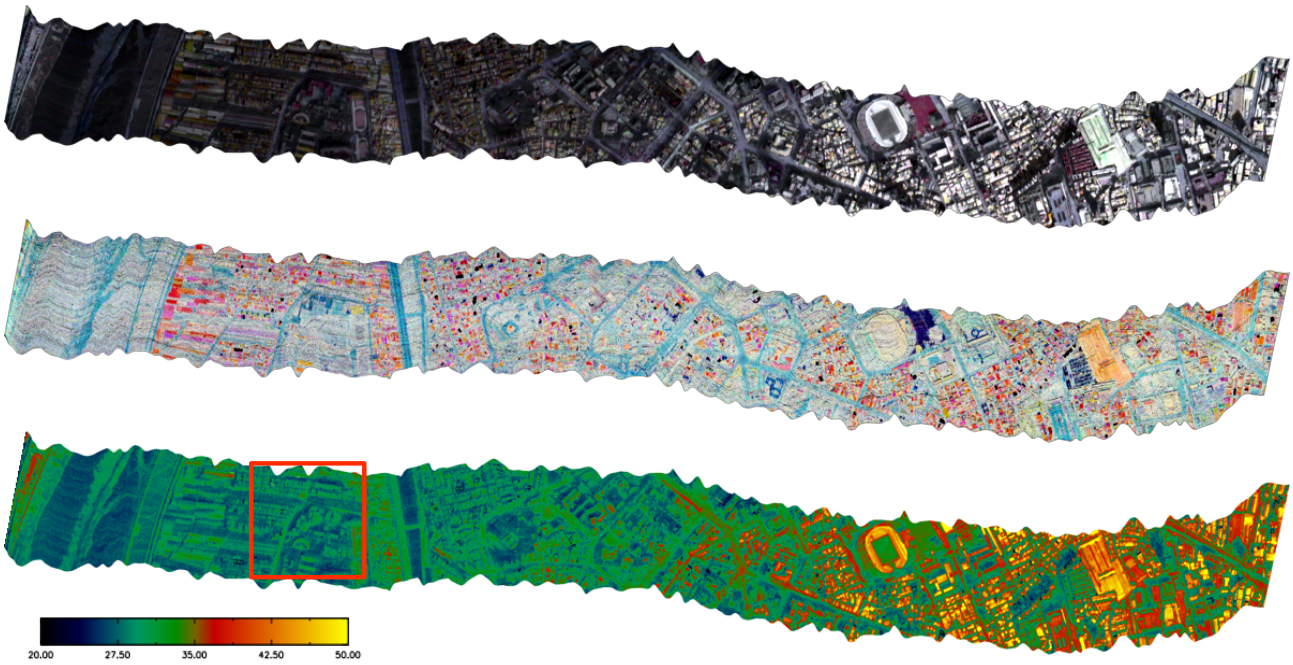

Figure 3. OWL scene of Taipei, Top: Spectral radiance (R:8.2, G:9.8, B: 11.2 μm), middle: spectral emissivity, same wavelengths; bottom: temperature ($20 - 50^{o}C$). Data courtesy of SPECIM Inc.

3. PROCESSING FLOW CHART

A general overview of the thermal image processing in DROACOR is illustrated in the flowchart in Figure 4. After reading (or providing) information about the image acquisition conditions like flight altitude, ground elevation, atmospheric conditions, most importantly water vapor content, the algorithm convolves the pre-computed entries in the LUT (c.f. Section 2.3) with the specific sensor response function. This is thereafter applied to the functions within DROACOR to the TIR images to retrieve surface temperatures and surface emissivities.

Input is a hyperspectral thermal infrared scene and the corresponding spectral response functions of the sensor. The hyperspectral data is to be calibrated to absolute spectral radiance to make it comparable to the physical simulations of the LUT. The data import is done semi-automatically using the meta data as provided by the sensor manufacturer. The outputs of DROACOR are: surface temperature map, the emissivity cube, the "cold" pixel map (if there are any), and optionally a mineral abundance map.

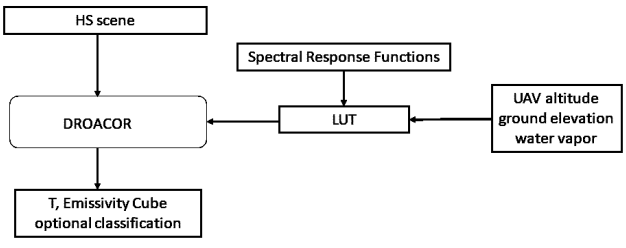

Figure 4. DROACOR flow chart.

4. RESULTS

Two examples are presented: the first is an urban application with a UAV data acquisition over a city to evaluate city temperatures and spectral emissivities of streets, building roofs, and to detect materials of low emissivity (e.g. glass and metal roofs). The second one presents a thermal hyperspectral scene acquired from a fixed ground-based platform with a horizontal scan system. This setup is often used for mineral applications, with an additional mineral classification based on the spectral emissivity features. However, such data acquisitions with horizontal geometry can also be employed in urban areas to analyze damages in buildings.

4.1 Urban application: city temperature, emissivity, low emissivity materials

Fig. 3 presents a hyperspectral scene of Taipei / Taiwan acquired by SPECIM's OWL sensor (https://www.specim.fi). The 102 spectral channels (7.8 to 12.5 μm, FWHM = 50 nm) were recorded November 15, 2015. The flight altitude was 760 m above ground, the average ground elevation is 20 m, and the ground sampling distance was GSD = 0.65 m. The figure shows the original spectral radiance and the emissivity output as false color display. Furthermore, the color coded surface temperature is depicted. The scene was recorded in the afternoon and the western part (left in image) was acquired under cloudy conditions. The highest temperatures can be found on roofs around the stadium visible to the west of the shown flight line.

Fig. 5 (top) shows the subset marked with a red square in Fig. 3. The middle part presents the temperature images for a zoom window (marked with a white square). As the cold pixel threshold *thc* increases from 0.70 to 0.85, an increasing number of pixels in the dark center is assigned a higher temperature according to Eq. 12.

The bottom part contains the corresponding cold pixel masks, where the calculated pixels are coded as 200 (white), and the

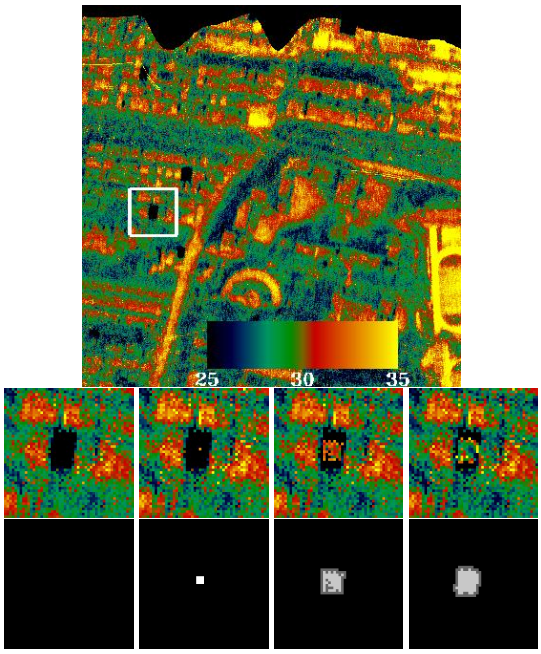

Figure 5. Top: Taipei subset temperature; middle: zoom for thc=0.70, 0.75, 0.80, 0.85; bottom: masks.

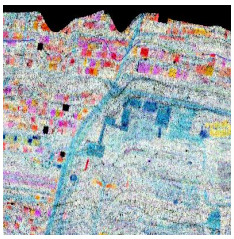

Figure 6. Subset emissivity ($RGB = 9.36,\ 10.33,\ 11.30\ \mu m$).

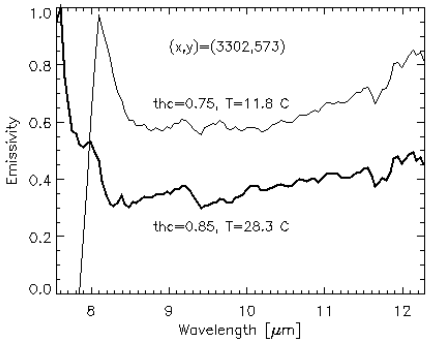

Figure 7. Sample of cold pixel emissivity and corrected emissivity spectrum.

neighboring pixels as 100 (dark grey). For the threshold *thc = 0.70* there are no cold pixels. For urban applications, the typical cold pixel threshold *thc* lies between 0.80 and 0.85. This threshold can be used to detect low emissivity surfaces and update their temperatures and emissivities according to section 2.2.

Fig. 6 shows the subset emissivity map corresponding to Fig. 5, and Fig. 7 presents a cold pixel emissivity spectrum (calculated with *thc=0.75*) and the corresponding corrected spectrum calculated with *thc=0.85*. The surface brightness temperature difference is 16.5°C, responsible for the updated spectrum.

4.2 Horizontal data acquisition: mineral identification

Fig. 8 (top) shows a Specim OWL scene acquired October 14, 2012. It contains a quartz- and silicates-rich hill and a gravel street in the foreground with some vegetation and the sky background. The spectral radiance (image 1 on top) is affected by the surface emissivity and temperature differences. These two effects can by distinguished after the temperature / emissivity separation with the NEM method. This separation is demonstrated in the 2nd image (spectral emissivity) and 3rd image (temperature).

The bottom figure presents the mineral classification based on the Spectral Angle Mapper (SAM, (Kruse et al., 1993)). SAM is a physically-based spectral classification that uses an n-D angle to match pixels to reference spectra. The algorithm determines the spectral similarity between two spectra by calculating the angle between the spectra and treating them as vectors in a space with dimensionality equal to the number of bands. For the mineral quantification product, the inverse of the spectral angle is used a proxy for mineral abundance such that higher values correspond to a better similarity to the reference spectrum. The results for a mapping between three mineral spectra (Goethite, Kaolinite, and Quartz) are shown. The abundance of a Kaolinite/Quartz background given by the purple color is visible while the kaolinite is visible as green spots in the false-color RGB display.

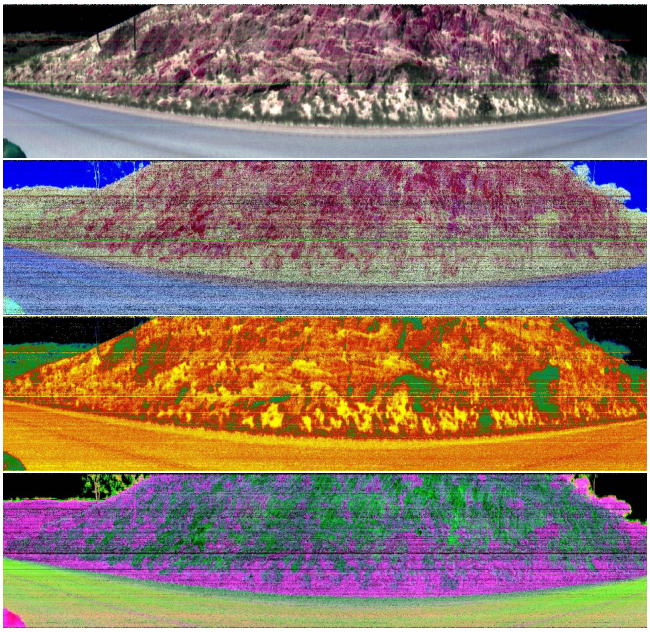

Figure 8. Scene with horizontal data acquisition. Top: spectral radiance, RGB= 10.9, 9.0, 8.1 μm, 2nd: spectral emissivity (RGB, same wavelengths), 3rd: temperature (scaled $30 - 60^o C$) bottom: inverse spectral angle mapping with R:Goethite, G:Kaolinite, B:Quartz.

5. DISCUSSION

The proposed method can be applied to single-band UAV calibrated imagery of the FLIR type, where a fixed scene emissivity (default $\varepsilon = 0.97$, typical for 8 - 13 μm broad-band FLIR)

has to be specified to calculate the surface brightness temperature. However, the main application fields exist for hyperspectral thermal imagers, where the normalized emissivity method is used to separate temperature and emissivity. In addition, we provide an algorithm to detect low emissivity materials ("cold" pixels) and iterate their temperature and emissivity. Here the critical parameter is the atmospheric water vapor. If this parameter is not available, it has to be taken from external sources, e.g., nearby meteorological stations, satellite data, or climatology.

A known problem with UAV based thermal hyperspectral imaging is the restricted data quality of the original imagery. Variable efficiency of single detector pixels often leads to visible banding, pixel dropouts and noisy image appearance (compare Fig. 8). Such artifacts are to be treated properly for improved results.

Another field of application exists for stationary horizontal ground based observations, where the hyperspectral camera is mounted on a platform, often including a wide angular scan system. This setup is normally employed for mining, but can also be used in urban applications (building damage, surface inspection), and agriculture (vegetation stress).

For mining we offer a spectral classification of the emissivity cube, where the user can select relevant library emissivity spectra. Figure 9 shows plots of currently supported emissivity spectra of minerals, taken from the John Hopkins University library included in ENVI (Harris Geospatial, 2021). This reference library may be adapted according to the needs of data users.

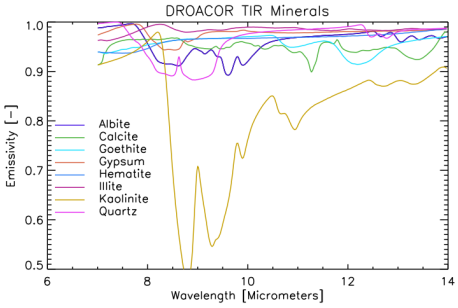

Figure 9. Emissivity spectra of minerals for standard inverse SAM mapping.

6. CONCLUSIONS

A method for the evaluation of thermal imaging spectrometer data acquired by drones is presented. It can be applied to UAV data of low altitudes (10 - 500 m) up to flight levels of 5 km above ground and elevations up to 4 km. It can also be used for fixed ground-based acquisitions with a horizontal view geometry and typical horizontal distances up to 500 m. The code is implemented in the IDL language (Harris Geospatial, 2021) and extends the DROACOR software of ReSe (Schläpfer et al., 2020) into the thermal spectral region.

It has been shown, that the developed method can retrieve the spectral emissivity and temperature at reasonable accuracy. The resulting products are limited by the availability of accurately calibrated and stable hyperspectral imaging systems. For drone based imaging, the quality of hyperspectral thermal infrared data is often affected by visible noise and banding artefacts. It is expected that data quality for the thermal infrared will improve in a similar way as it did with VNIR/SWIR systems in the past years such that noise can be reduced and more information may be revealed from the imagery. In the meantime, some additional focus is to be put on data quality improvements by appropriate filtering and spectral polishing.

However, a step forward in thermal drone data processing has been made by the development of an operationally usable and flexible physical atmospheric correction method which is applicable to various kinds of thermal imagers and which is flexible enough to support upcoming instruments.

ACKNOWLEDGEMENTS

We are grateful to Specim for providing the OWL scenes.

REFERENCES

Harris Geospatial, 2021. IDL/ENVI. https://www.l3harrisgeospatial.com.

ITRES Research LImited, 2019. TASI-600 Thermal Hyperspectral Imaging Sensor. 1–2. https://itres.com/wp-content/uploads/2019/09/TASI600.pdf.

Kahle, A., Madura, D., Soha, J., 1980. Middle infrared multispectral aircraft scanner data analysis for geological applications. *Applied Optics*, 19, 2279–2290.

Kruse, F. A., Lefkoff, A. B., Boardman, J. W., Heidebrecht, K., Shapiro, A., Barloon, P. J., Goetz, A. F. H., 1993. The spectral image processing system (SIPS)—interactive visualization and analysis of imaging spectrometer data. *Remote Sensing of Environment*, 44, 145 – 163. https://www.sciencedirect.com/science/article/pii/003442579390013N.

Mayer, B., Kylling, A., Emde, C., Buras, R., Hamann, U., Gasteiber, J., Richter, B., 2019. libradtran user's guide, version 2.0.3. available from: http://www.libradtran.org/doc/libRadtran.pdf.

Realmuto, V. J., 1990. Separating the effects of temperature and emissivity: emissivity spectrum normalization. *Proc. 2nd TIMS Workshop*, JPL Publ. 90-55, 31–37.

Schläpfer, D., Popp, C., Richter, R., 2020. Drone Data Atmospheric Correction Concept for Multi- and Hyperspectral Imagery – the DROACOR Model. *ISPRS - International Archives of the Photogrammetry*, XLIII-B3-2020, 473–478.

Schläpfer, D., Richter, R., Popp, C., Nygren, P., 2021. DROACOR Reflectance Retrieval for Hyperspectral Mineral Exploration Using a Ground-Based Rotating Platform. *ISPRS - International Archives of the Photogrammetry*, XLIII-B3-2021, 209–214.

SPECIM Spectral Imaging Ltd., 2021. Aisa OWL. https://www.specim.fi/products/OWL/.

Teledyne FLIR, 2021. FLIR-Duo Pro R. https://www.flir.de/support/products/duo-pro-r/.

TELOPS, 2022. Telops Hyperspectral Cameras - Hyper-Cam HS-IR. 1–4. https://www.telops.com/products/hyperspectral-cameras.